Geomorphology 389 (2021) 107799

Contents lists available at ScienceDirect

Geomorphology

journal homepage: www.elsevier.com/locate/geomorph

Automating coastal cliff erosion measurements from large-area LiDAR datasets in California, USA

Zuzanna M. Swirad *, Adam P. Young

Scripps Institution of Oceanography, University of California San Diego, 9500 Gilman Dr., La Jolla, CA 92093, USA

ARTICLE INFO

Article history:
Received 17 December 2020
Received in revised form 29 April 2021
Accepted 20 May 2021
Available online 27 May 2021

Keywords:
Coastal cliffs
Landslides
Topographic change detection
Machine learning

ABSTRACT

Quantifying coastal cliff erosion is critical for improved predictions of coastal change and coastal management. However, few studies have been conducted at a scale (>100 km) and resolution (~1 m) sufficient to constrain regional change. Here, we quantified cliff erosion for 866 km of the California coastline using airborne LiDAR data collected in 2009–2011 and 2016. A semi-automated method was used to map cliff faces. Negative (volume loss) and positive (volume gain) change objects were created by grouping adjacent cells using vertical and areal change thresholds and surface optical signatures. We assessed the performance of five machine learning algorithms to separate erosion and deposition from other changes within the cliff face, notably vegetation loss and growth, and found that discriminant analysis performed best. After applying the classification method to the entire cliff change dataset, the results were visually inspected for quality control, producing a final dataset comprised of 45,699 erosion and 1728 deposition objects. The net volume loss from 2009–2011 to 2016 was 1.24×10^7 m^3, equivalent to an erosion rate of 2.47 m^3 yr^{-1} per meter of coastline, and an average cliff retreat rate of 0.06 m yr^{-1}. Eroded volumes ranged from 6.43 m^3 to 7.52×10^5 m^3 and fit a power-law frequency distribution ($\beta = 0.80$; $r^2 = 0.99$). Over this study period, 7% of eroded material remained on the cliff face. Cliff retreat rates varied spatially with the highest rates in Humboldt County (0.18 m yr^{-1}) and the lowest in Orange County (0.003 m yr^{-1}).

1. Introduction

Coastal cliffs are erosional features found worldwide (Emery and Kuhn, 1982; Trenhaile, 1987; Sunamura, 1992; Prémaillon et al., 2018; Young and Carilli, 2019) and their retreat threatens clifftop communities and infrastructure. Sea level rise and increased storminess associated with climate change are expected to increase cliff erosion (Slott et al., 2006; Ashton et al., 2011). Quantifying cliff retreat and understanding the driving processes is essential for improved coastal management and coastal erosion projections (Walkden and Dickson, 2008; Limber et al., 2018). Cliffed coastlines are less studied than other coastal environments (Naylor et al., 2010) and only a few studies (Hapke et al., 2009; Young, 2018) provide analysis at large spatial scales (>100 km) that can help inform regional planning and decision making.

Historical cliff retreat rates are often manually measured on cliff top transects using historical maps and aerial photography (e.g. Clark and Lee, 2002; Brooks and Spencer, 2010). However, cliff top changes may not represent cliff face changes (Rosser et al., 2005; Young et al., 2009), are subject to mapper interpretation, and are limited to the relatively low resolution of historical data that often results in high measurement uncertainty (Moore, 2000; Lim et al., 2010). Recently, several studies developed methods to automate detection of cliff bases and tops to avoid bias associated with mapper interpretation (Liu et al., 2009; Richter et al., 2013; Palaseanu-Lovejoy et al., 2016; Payo et al., 2018). Liu et al. (2009) approximated coastal bluff base and top positions using slope variations along shore-perpendicular transects, combined with image segmentation, surface reconstruction, and edge detection on ortho-images. Richter et al. (2013) identified the beach/dune border directly on digital elevations models (DEMs, without using transects), as a contour line created using Sobel (1st derivative) and Laplacian (2nd derivative; sensitive to slope change) terrain filters. Palaseanu-Lovejoy et al. (2016) developed a simple cliff delineation model by comparing elevations along a cross-shore transect with elevations along a straight line between transect ends. Cliff base and top points were defined as locations along the transects with the largest difference between the two elevations. Payo et al. (2018) used the same principle but also developed automated generation of the coastline and transects, and extraction of elevations along the transects.

Advances in mapping with Light Detection and Radar (LiDAR) and Structure-from-Motion (SfM) photogrammetry allow for 3D erosion analysis using point clouds (e.g. Williams et al., 2018; Warrick et al., 2019; Benjamin et al., 2020) and 2.5D analysis using DEMs (e.g. Young and Ashford, 2006; Young et al., 2009, 2011, 2021; Earlie et al., 2015;

* Corresponding author.
E-mail address: zswirad@ucsd.edu (Z.M. Swirad).

https://doi.org/10.1016/j.geomorph.2021.107799

Letortu et al., 2015; Terefenko et al., 2019; Westoby et al., 2020). These methods allow the identification and analysis of erosion and deposition zones (Young, 2018), cliff face erosion sequences (Collins and Sitar, 2008; Rosser et al., 2013), and cliff failure volume-frequency relationships (Benjamin et al., 2016, 2020; Williams et al., 2018, 2019). Existing 2.5D/3D studies often span shorter study durations (up to a decade) but provide higher resolution analysis compared to studies based on historical cartography.

Volumetric topographic change analysis is limited by data quality, resolution, surface complexity, and the ability to isolate valid cliff change (Milan et al., 2011; Williams, 2013; Turowski and Cook, 2017). Differenced coastal terrain models can show a combination of changes related to dune morphology, beach dynamics, cliff erosion, human modification, vegetation, etc. To isolate valid cliff erosion, topographic changes are often categorized manually (Young, 2018). Machine learning algorithms provide a method to automate this classification, reducing human-induced classification error, and increasing processing efficiency (Alpaydin, 2014). One such method, object-based image analysis, segments rasters into pixel groups (objects) by maximizing the similarity within object classes (Blaschke, 2010). Example applications in geomorphology include land cover classification (Li et al., 2013; Juel et al., 2015; Liu et al., 2018), landslide mapping (Li et al., 2015; Amatya et al., 2019; Ghorbanzadeh et al., 2019), and building landslide susceptibility models (Marjanović et al., 2011; Goetz et al., 2015; Dickson and Perry, 2016). To our knowledge, machine learning has not previously been used to classify erosion and deposition within cliff faces.

The primary focus of this study was to develop a method to quantify coastal cliff erosion at high-resolution over large spatial areas. This was achieved through semi-automated delineation of coastal cliff faces from terrain models, and the application of machine learning algorithms to classify changes within the cliff face to generate an inventory of erosion and deposition features. This study was primarily focused on developing and validating these new methods, but we also quantified change magnitudes such as volume and retreat rates, explored volume-frequency distributions, and examined alongshore erosion differences at county level and in 10 km alongshore blocks. Higher resolution spatio-temporal variability in erosion and controlling factors will be examined with this dataset in a subsequent study.

2. Study area

Rocky and cliffed coasts comprise 72% of California's 1646 km coastline (Fig. 1, Griggs et al., 2005; Young, 2018). The California coast is tectonically active and contains numerous fault zones, most notably the San Andreas Fault, dividing the North American and Pacific plates. Tectonic processes have produced several coastal mountain ranges and a series of uplifted marine terraces along much of the coastline. The coastal cliff lithology includes granite, Tertiary sandstones, shales and conglomerates, Mesozoic sandstone, shales and basalts, and weakly-lithified Quaternary deposits (Hapke et al., 2014). In southern and central California, the mean cliff base Schmidt hammer rebound value (a measure of rock hardness), measured mostly in Tertiary sedimentary and shale cliffs, was 28 ± 13 (std dev) and ranged from 6 to 71 (Young, 2018).

Shore platforms fronting the cliffs are usually covered by a veneer of beach sand and sometimes cobble (Griggs et al., 2005; Hapke et al., 2014). Vos et al. (2020) estimated mean state-wide beach slope of 0.068 ± 0.024 (std dev) from satellite data on >8000 transects. Beach

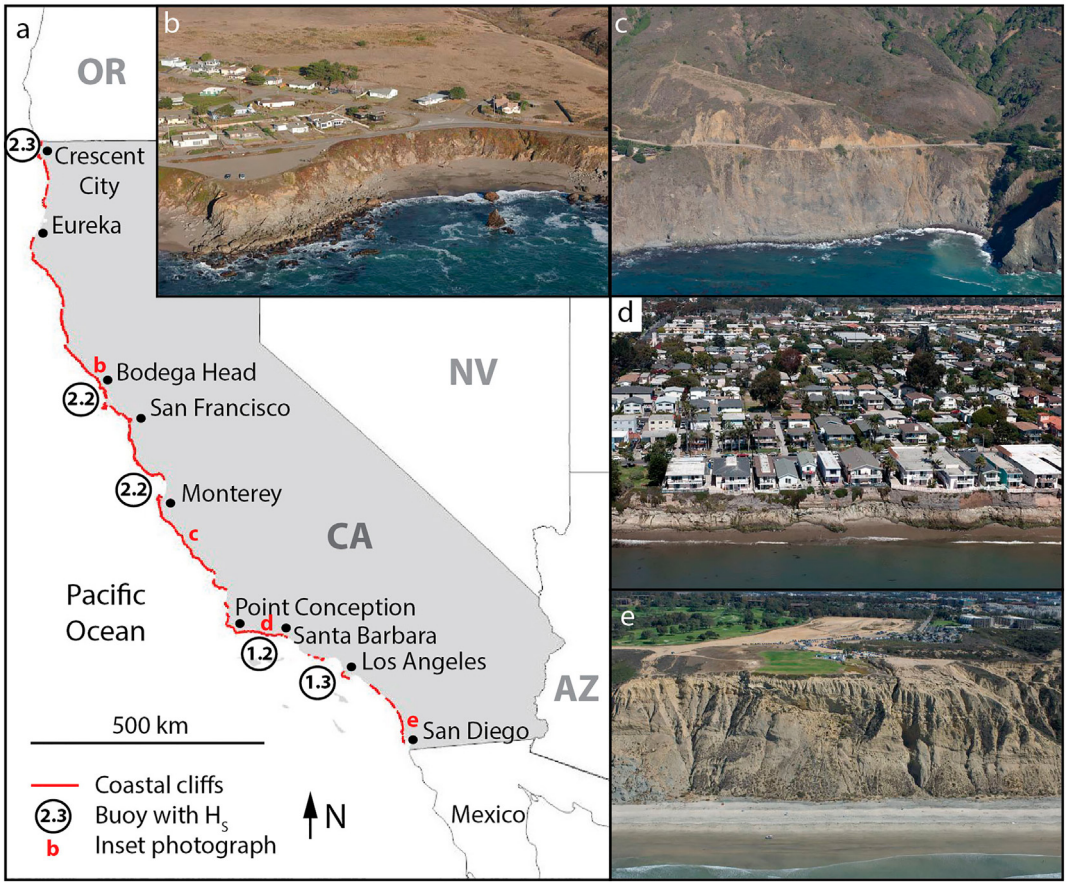

Fig. 1. California study area showing a) the distribution of coastal cliffs (red) and (b-e) examples of coastal settings: b) uplifted marine terrace in Bodega Head; c) coastal cliff as part of a mountain slope in Big Sur; d) developed cliff tops in Isla Vista, Santa Barbara; e) uplifted marine terrace in Torrey Pines, San Diego. H_S refers to the average significant buoy wave height from 1982–2008. Photographs copyright © 2002–2021 Kenneth & Gabrielle Adelman, California Coastal Records Project, www.Californiacoastline.org.

width ranges from 0 to hundreds of meters and varies spatially and seasonally depending on tidal levels, wave conditions, sand elevation, etc.

The California coast is exposed to waves generated by local winds and distant storms in both hemispheres. During winter, swell from the North Pacific and Gulf of Alaska is most energetic, whereas swell from the South Pacific dominates in summer. Waves reaching the southern California coast undergo a complex transformation, and shadows of the Channel Islands create strong alongshore variations in wave height (Pawka, 1983). Annual nearshore wave energies are generally larger north of Point Conception in central and northern California compared to southern California. For example, between 1982 and 2008 the average significant buoy wave height south of Point Conception at Santa Monica (#46025) and Santa Barbara (#46053) was 1.2–1.3 m, compared to 2.2–2.3 m north of Point Conception at Monterey (#46042), Bodega Bay (#46013), and Crescent City (#46027) (Fig. 1a; ndbc.noaa.gov). Tidal range is about 1.6–2.1 m (tidesandcurrents.noaa.gov). Tide level and beach elevation influence wave-cliff interaction in some portions of the state, where large swells arriving during relatively low tides may not reach the cliffs, whereas moderate swell arriving during high tide can have significant wave-cliff impact duration (Young et al., 2016).

The California climate is characterized by dry summers and occasionally wet winters, with most rainfall occurring from November to March. Annual coastal precipitation generally increases northward with mean annual precipitation ranging from 257 mm in San Diego to 1798 mm in Crescent City, but is locally higher along the Big Sur coast and lower in the San Francisco and Monterey areas (wrcc.dri.edu).

Coastal cliff retreat studies in California date back at least to 1932 (Vaughan, 1932). Since then, numerous studies have been conducted using a variety of measurement techniques ranging from observations of dated inscriptions (Emery and Kuhn, 1980) to terrestrial LiDAR (Collins and Sitar, 2008) and Unmanned Aerial Vehicle based SfM (Warrick et al., 2019). These studies have been often local, but Griggs et al. (2005) provided a statewide compilation of many of these studies, and U.S. Army Corps of Engineers (1971) provided a qualitative statewide erosion assessment. Hapke et al. (2009) measured cliff top retreat along 353 km cliffs (~20% of California coastline) using National Ocean Service Topographic Maps ('T-sheets') from the 1920s–1930s and airborne LiDAR collected in 1998 and 2002. Using shore-normal transects spaced 20 m alongshore, Hapke et al. (2009) calculated mean and maximum cliff top retreat rates of 0.3 m yr^{-1} and 3.1 m yr^{-1}, respectively, with estimated errors of 0.2 m yr^{-1}. Young (2018) conducted the most recent systematic study measuring cliff changes for 595 km of southern and central California (~35% of California coastline) in 5 m alongshore compartments. Using airborne LiDAR collected in 1998 and 2009–2011, Young (2018) measured a mean cliff top retreat rate of 0.12 m yr^{-1} (max 4.2 m yr^{-1}) and a cliff face retreat rate (based on 2.5D change analysis) of 0.04 m yr^{-1} (max 3.8 m yr^{-1}). Young (2018) found that historical (1920s–1930s to 1998) and more recent (1998 to 2009–2011) cliff top retreat rates were significantly inversely correlated for areas with large retreat rates in either epoch.

3. Methods

The workflow to develop inventories of erosion and deposition objects consisted of four linked modules including point cloud processing, cliff face mapping, change detection, and change classification (Fig. 2).

3.1. Data preparation

3.1.1. Data acquisition

This study used freely available airborne LiDAR survey data collected in 2009–2011 and 2016 (coast.noaa.gov). The 2009–2011 survey (NOAA "CSC") was conducted on 51 days between October 2009 and August 2011. For this survey, the coastline was split into 22 alongshore blocks, each of which was surveyed over single or multiple days, with timespans usually less than a few months but reaching >200 days in northern California (Table 1). The point clouds have a vertical reference of NAVD88 and Geoid09, and horizontal datum of NAD83(NSRS2007). The average point density is 1.5 pts. m^{-2}. The vertical accuracy (at the 95% confidence level) varies with terrain type and equals 0.07 m for urban areas, 0.09 m for open terrain, 0.23 m for marsh, and 0.40 m for grass, weeds, and crops (Dewberry, 2012).

The 2016 survey (USGS "West Coast El Niño") was conducted in April–May 2016 along the coast of California, Oregon, and Washington. Tiled ~1 km^2 point clouds are vertically referenced to NAVD88 and Geoid12B, and horizontal datum NAD83(2011). The average point density is 66 pts. m^{-2}. The horizontal accuracy is 0.21 m, and the vertical accuracy is 0.11 m and 0.21 m, for non-vegetated and vegetated terrain, respectively (95% confidence level; Dewberry, 2016).

3.1.2. Point cloud processing

Each survey dataset was separated into 60 predefined cliffed alongshore sections ranging from 6 to 51 km using a polygon shapefile. Where possible, section ends were placed at non-cliff locations, such as estuary mouths. Ground filters were not used. Point clouds were inspected for outliers. Using CloudCompare, we established optimized parameters (points over one standard deviation from the average distance between the 30 nearest points) to identify and remove erroneous points such as birds and vehicles without losing ground points. The subsequent data processing was performed in ArcMap 10.5, ArcGIS Pro 2.4, and MATLAB R2019a. We randomly subsampled 20% of the 2016 data points to reduce processing time, and because the high point density was not necessary considering the relatively low resolution of the 2009–2011 dataset. Subsampling did not generate scarce cliff face coverage, because the cliff regions typically had the highest original point density. Next, each section was converted to triangulated irregular networks (TINs) and TIN facets with edges longer than 5 m were removed. TINs were converted into 1 m resolution DEMs using a natural neighbor interpolation (Sibson, 1981). The DEM resolution was selected based on the lower resolution point density (1.5 pts. m^{-2}; 2009–2011), as pixel values should be interpolated from more than one point to minimize error (Wheaton et al., 2010).

3.1.3. Cliff face identification

Complex and variable cliff topography in the study area limited direct use of existing independent cliff base and top identification methods (Liu et al., 2009; Richter et al., 2013; Palaseanu-Lovejoy et al., 2016; Payo et al., 2018). Therefore, to delimit the cliff face, we developed a semi-automated method to extract both the cliff base and cliff top from terrain models (Fig. 3) using combined elements from existing studies (Liu et al., 2009; Richter et al., 2013; Swirad and Rees, 2015; Palaseanu-Lovejoy et al., 2016; Swirad et al., 2016; Payo et al., 2018) that search for characteristic inflection points on shore-normal profiles.

In ArcMap, we generated shore-normal transects at 5 m alongshore intervals along a generalized shoreline GIS layer from the California Department of Fish and Wildlife (purl.stanford.edu/hj484bt5758). Using a generalized shoreline helps generate orderly, non-overlapping transects. Transects extended 100 m seaward and 300 m landward from the generalized shoreline, or to the first paved road (www.openstreetmap.org; as of 28 Apr 2020), to ensure entire cliff faces were within the buffer, and were sampled at 1 m cross-shore spacing.

Next, we manually labelled cliff base and top locations on 5558 transects (~2.5% all transects) and extracted the associated attributes of the 1) distance to the seaward end of the transect (ArcMap *Near* tool), 2) elevation, 3) convolution Laplacian filter value (ArcMap *Extract Values to Points* tool), 4) average slopes of 10 adjacent seaward and landward points (optimized based on typical cross-shore cliff extent of >10 m), and 5) vertical difference between the transect and a trendline, i.e. a straight line connecting transect ends (calculated in MATLAB). Thresholds for automated cliff base and top selection were set based on the attribute ranges of the manually labelled points. Potential cliff

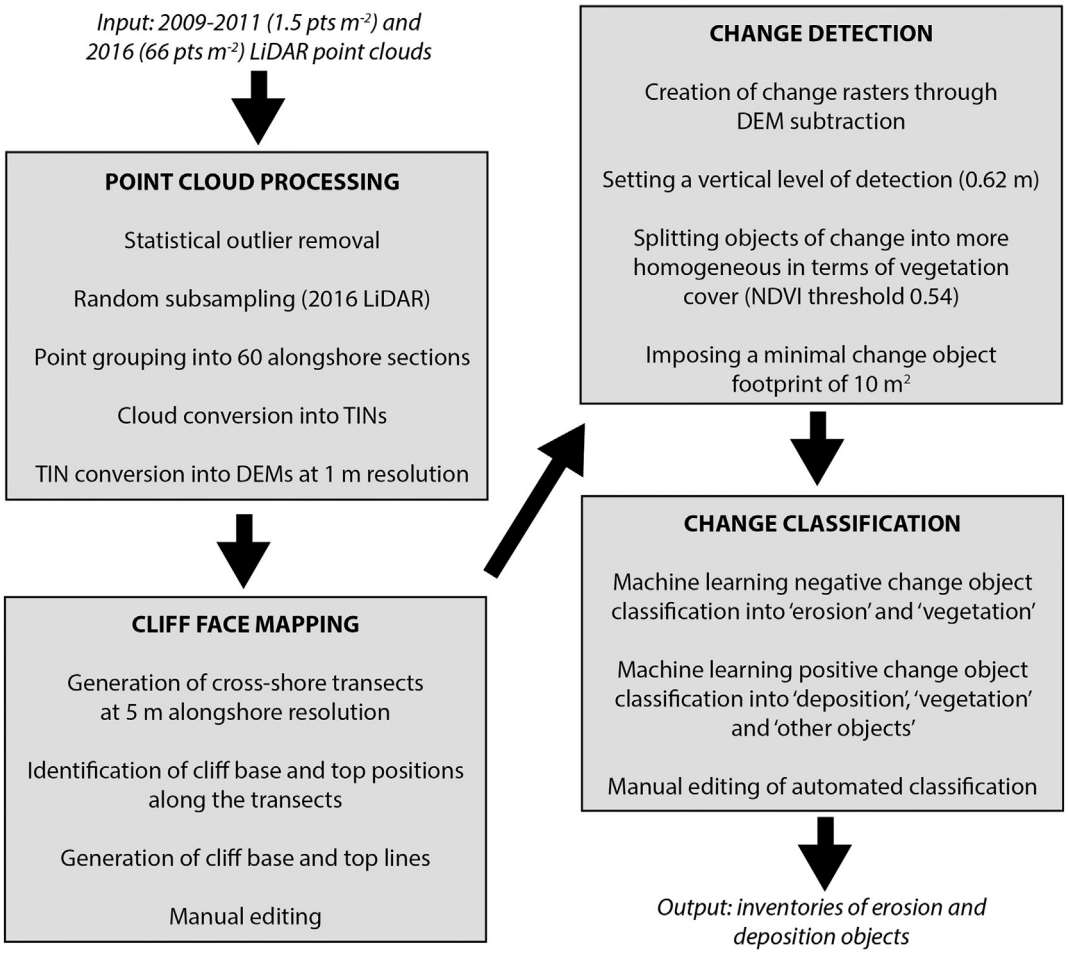

Fig. 2. Workflow to create inventories of erosion and deposition objects within cliff faces from LiDAR point clouds between 2009–2011 and 2016 in California. Acronyms: TIN – triangulated irregular network; DEM – digital elevation model; NDVI – normalized difference vegetation index.

Table 1
2009–2011 LiDAR survey extents, block identifiers, and dates (Fugro, 2011). The timespan used for the erosion analyses was calculated between the latest 2009–2011 survey date and April–May 2016. Alongshore extent was measured from the USA/Mexico border (0 km) to the California/Oregon border (1646 km).

Alongshore extent (km)	Survey date (block ID from Fugro, 2011)	Analysis timespan (yr)
0–49	Nov 2009 (V)	6.6
49–133	Oct 2009 (U)	6.6
133–184	Oct 2009 (T)	6.6
184–284	Oct 2009 (S)	6.6
284–379	Nov 2009 (R)	6.5
379–423	Nov 2009 (Q)	6.5
423–467	Nov 2009 (P)	6.5
467–555	Nov 2009 (O)	6.5
555–627	Nov 2009; May 2010 (N)	6.0
627–675	Nov 2009 (M)	6.5
675–768	Nov 2009; May 2010 (L)	6.0
768–848	May 2010; Jun 2010; Oct 2010 (K)	5.6
848–913	Jun 2010; Sep 2010; Oct 2010 (J)	5.6
913–984	Jun 2010; Sep 2010; Nov 2010 (I)	5.6
984–1015	Jun 2010; Oct 2010; Nov 2010 (H)	5.6
1015–1118	Sep 2010; Oct 2010; Nov 2010 (G)	5.6
1118–1202	Sep 2010; Nov 2010 (F)	5.6
1202–1297	Sep 2010; Oct 2010; May 2011 (E)	5.0
1297–1388	Oct 2010; May 2011; Jun 2011 (D)	5.0
1388–1458	Jun 2011; Jul 2011; Aug 2011 (C)	4.8
1458–1573	Sep 2010; May 2011; Jun 2011; Aug 2011 (B)	4.8
1573–1646	Sep 2010; Nov 2010; Dec 2010; Jun 2011; Jul 2011 (A)	4.9

base points met the following criteria: 1) location 80–200 m from the seaward transect end, 2) elevation 0–4 m NAVD88, 3) average slope of the 10 adjacent seaward vertices <20°, 4) average slope of the 10 adjacent landward vertices >15°, and 5) elevation at least 8 m below trendline 1 (blue line and *h1* in Fig. 3b). If more than one point fulfilled all criteria, the point with the lowest convolution Laplacian filter value was selected (after Richter et al., 2013). If no points fulfilled the criteria, the transect was skipped. The cliff base line was generated by connecting available ordered cliff base points.

Potential cliff top points met the following criteria: 1) location >100 m from the seaward transect end, 2) elevation 15–100 m NAVD88, 3) average slope of the 10 adjacent seaward vertices >10°, 4) average slope of the 10 adjacent landward vertices <40°, and 5) elevation above trendline 2 (dashed line and *h2* in Fig. 3b). If more than one point fulfilled all the criteria, the point with the greatest *h2* was selected.

The automated mapping correctly identified the same manually labelled transect point location for 90% (5002) of cliff base and 71% (3946) of cliff top points, and was then applied over the entire coastline. Cliff base and top positions were visually inspected and manually modified if necessary.

The cliff base and top points delimited the cliff face area. Merged cliff face areas from the two surveys defined the area of interest for change detection with the seaward extent usually representing the 2009–2011 cliff base (except locations where deposition in 2016 was more seaward) and the 2016 cliff top as the landward extent (Fig. 3c). Areas with errors, insufficient data in either survey, or significant geodetic offset between the surveys (Martin, 2012) were masked out, which accounted for 14% of the mapped cliff face area.

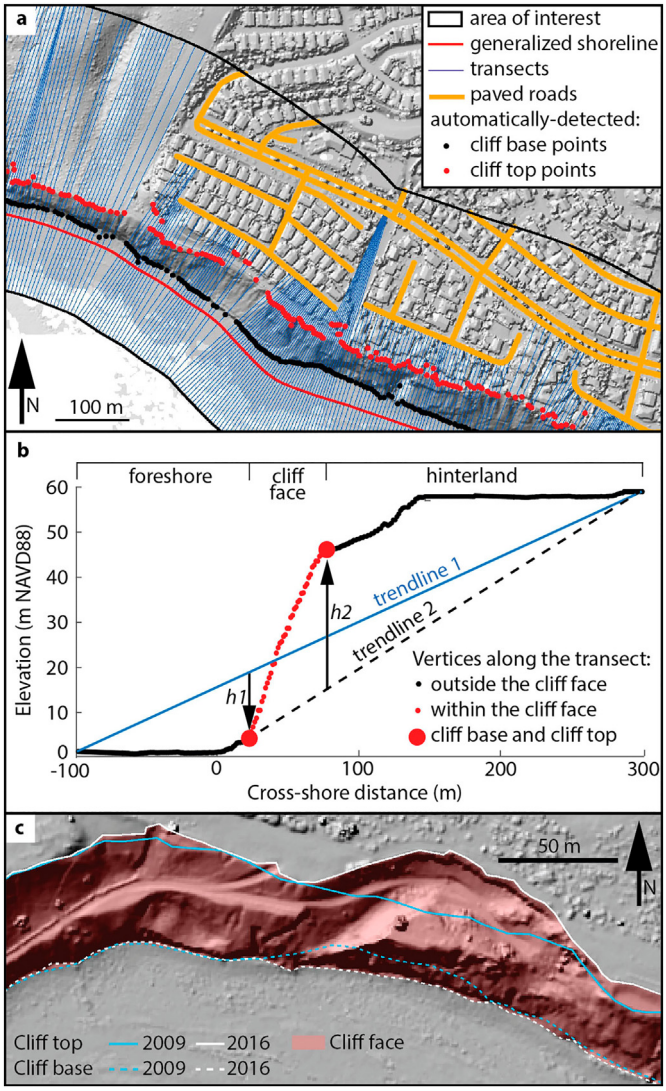

Fig. 3. Cliff face identification: a) example of cross-shore transects and automatically identified (before manual editing) cliff base and cliff top points (background: 2016 LiDAR hillshade); b) characteristics of vertices along a transect (h1 and h2 indicate differences in elevation used in automated detection of the cliff base and top, respectively); c) example of the final mapped cliff face extent (background: 2016 LiDAR hillshade).

3.1.4. Change object inventories

Topographic change detection consisted of several steps (Fig. 4). First, DEM rasters were differenced (ArcMap *Minus* tool) to show negative and positive elevation change. Changes included both real change (i.e. topography and vegetation) and erroneous change from survey inaccuracy, interpolation, and geodetic offset (Martin, 2012; Williams, 2013; Turowski and Cook, 2017).

Twenty control areas spread throughout the study area were used to establish a vertical level of detection delimiting lower-magnitude elevation changes indistinguishable from noise. Control areas consisted of inland slopes (average slope 14–36°; range 0–57°) representative of the coastal cliff topography and vegetation conditions (using the Normalized Difference Vegetation Index, NDVI; range 0.25–0.83) obtained from 2009 optical imagery (National Agriculture Imagery Program, NAIP imagery, gis.data.ca.gov), and were inspected to confirm no significant valid change occurred during the study period. The vertical root mean square difference (RMSZ) between surveys for the control areas ranged between 0.07 and 0.32 m (Table 2). We established a vertical level of detection threshold of 0.62 m (1.96 × max control area RMSZ at 95% confidence level) and grouped adjacent grid cells into positive (change raster values ≥ 0.62 m) and negative (change raster values ≤ − 0.62 m) change objects.

Change objects were divided into smaller regions of similar vegetative surface conditions based on a 0.54 NDVI threshold (Fig. 4) determined using 100 non-vegetated and 100 vegetated manually classified objects (Fig. 5) using the 2009 NAIP optical imagery (gis.data.ca.gov). Lastly, we enforced a minimal change object footprint of 10 m^2 based on analysis of the 20 control areas, limiting volume detection to ≥6.2 m^3. This produced an inventory of 52,862 positive and 94,130 negative change objects meeting vertical and areal thresholds (Fig. 4).

3.2. Object classification

3.2.1. Selection of predictors and algorithms

Change objects were classified to separate cliff erosion and deposition from other changes within the cliff face such as vegetation loss and growth, dune dynamics, and construction activities. We characterized each change object with multiple attributes (with ArcMap tools), henceforth referred to as 'predictors' (Table 3). We selected 11 predictors for erosion, and 13 for deposition related to location, topography, optical signature, size, and shape, based on field observations and characteristics that could help distinguish mass movements from other change, mainly the vegetation loss and growth. Predictors of object distance from the cliff base and cliff top, and elevation were used because vegetation is often located in higher landward sections close to the cliff top while deposition objects are often located at or near the cliff base at lower elevations. Footprint area and vertical change predictors help identify large scale coastal change because vegetation change is typically smaller scale. For example, erosion objects can include elevation change up the cliff height and can reach >200 m, while vegetation change is limited to relatively low vegetation heights (though some sections of northern California contain giant sequoias that can reach >50 m). Slope and roughness predictors represent variability in object 'topography' and help separate complex tree crowns and bush top surfaces from smoother erosion and deposition surfaces. Similarly, topographic aspect predictors are more consistent for erosion and deposition objects than vegetation. NDVI predictors provide a direct measure of vegetation, however, they may not work well for identification of sparse vegetation areas or mass movements that include vegetated surfaces. The width to length ratio shape predictor helps identify extended alongshore sections where the entire cliff face receded (low ratio). Deposition objects are often located close to and seaward of erosion objects. Therefore, two erosion-related predictors were used for deposition detection including distance and direction to nearby erosion objects. Some predictors include multiple metrics (e.g. min, max, range) to account for variability. For example, to distinguish a landslide from a tree failure, range and standard deviation of elevation may be more important than the absolute elevation.

Using MATLAB, we tested five machine learning classification algorithms: *k*-nearest neighbors (number of neighbors, *k* programmatically picked from $k = 1{:}50$ based on the test loss; Euclidean distance), decision trees, naïve Bayes (normal kernel density distribution), discriminant analysis, and support vector machines (polynomial kernel function; standardized predictors) (Alpaydin, 2014). We selected these algorithms because they allow object classification from topographic and optical predictors, and have been used previously for classifying landslides (Marjanović et al., 2011; Goetz et al., 2015; Dickson and Perry, 2016). The algorithms vary in terms of sensitivity to known data, assumptions about the character of input parameters and thresholds for grouping. The *k*-nearest neighbors algorithm ascribes object class based on the proximity to labelled metrics. It is sensitive to known data including outliers. The decision trees method makes a series of binary splits with thresholds optimized to minimize variance. Excessively complex trees may over-fit data, while datasets with unbalanced classes may create bias. The naïve Bayes algorithm applies the Bayes theorem that

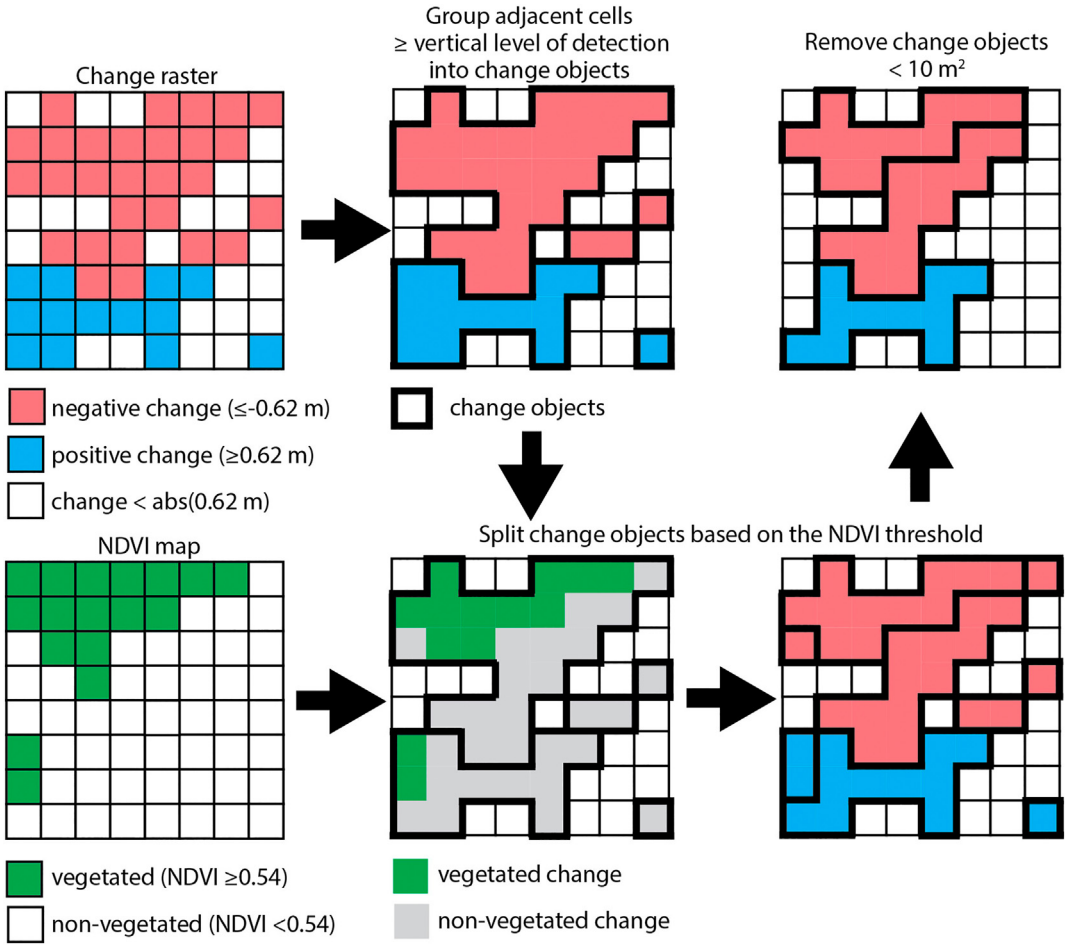

Fig. 4. Topographic change detection workflow. The vertical level of detection for differences in DEMs was set to 0.62 m. The Normalized Difference Vegetation Index (NDVI) threshold was set to 0.54.

describes probability of event from the prior knowledge of conditions, and assumes predictor independence. Discriminant analysis assumes that the observations in each class can be modelled with a multi-dimensional normal probability. The boundary between classes is based on the statistical distribution, which makes the method less dependent on the training data noise compared to other algorithms. Limitations of discriminant analysis include assumptions of multivariate normality, equality of covariance matrices, and linearity. The support vector machines algorithm attempts to maximally separate classes by finding a vector with the lowest error or maximum separation. That method may not be suitable if the margin of separation is narrow (Alpaydin, 2014).

Table 2
Control areas used to estimate vertical errors (RMSZ – root mean square difference).

UTM zone N	Centroid X (m)	Centroid Y (m)	Area (m^2)	Change raster value (mean ± std dev) (m)	RMSZ (m)
11	477,257	3,614,730	4964	−0.22 ± 0.09	0.24
11	475,604	3,644,384	1147	−0.03 ± 0.17	0.18
11	459,375	3,680,254	10,745	−0.14 ± 0.05	0.15
11	424,061	3,713,249	2853	−0.03 ± 0.13	0.14
11	352,788	3,767,942	3816	−0.21 ± 0.07	0.22
11	311,924	3,773,632	6166	−0.18 ± 0.13	0.22
11	244,808	3,811,839	5981	−0.15 ± 0.04	0.16
10	732,358	3,814,883	4290	−0.12 ± 0.14	0.19
10	716,241	3,885,242	514	−0.11 ± 0.06	0.12
10	666,889	3,944,425	4632	−0.07 ± 0.05	0.09
10	599,461	4,020,353	2964	−0.01 ± 0.12	0.12
10	575,261	4,093,193	2272	0.02 ± 0.07	0.07
10	552,936	4,129,960	12,705	0.06 ± 0.09	0.11
10	544,695	4,169,815	12,510	0.03 ± 0.15	0.15
10	500,044	4,238,538	26,248	−0.19 ± 0.10	0.21
10	439,248	4,306,235	20,074	−0.13 ± 0.07	0.15
10	429,468	4,397,206	4042	−0.26 ± 0.07	0.27
10	406,775	4,438,242	695	−0.31 ± 0.04	0.32
10	384,567	4,469,860	8736	−0.05 ± 0.05	0.07
10	411,008	4,592,439	2955	0.10 ± 0.21	0.23

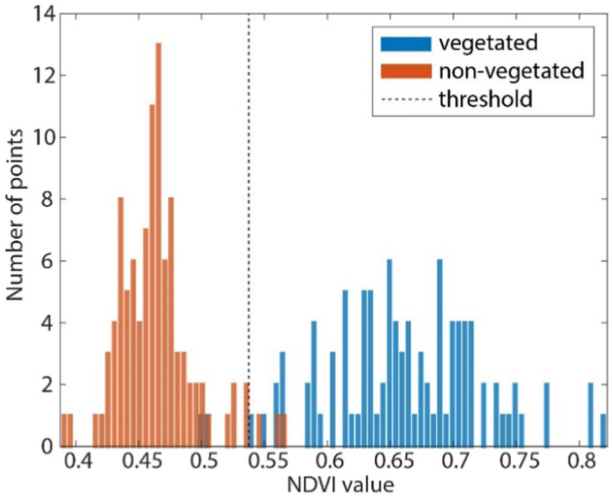

Fig. 5. The NDVI (Normalized Difference Vegetation Index) threshold of 0.54 was selected, which generally separated 100 vegetated and 100 non-vegetated classified areas.

3.2.2. Cliff erosion

To classify negative changes, we used 1000 randomly selected objects, manually classified as 'erosion' or 'vegetation'. Of the 1000 manually classified negative-change objects ('known-class'), 13 were excluded from modelling because they contained erroneous survey artifacts or exceeded 1500 m^3 (objects >1500 m^3 were assumed to exclusively represent cliff erosion). We randomly split the manually classified inventory into training (70%) and test (30%) sets and examined the five machine learning algorithms using 11 predictors (Table 3). Based on the proportion of misclassified objects in the test set (henceforth referred to as 'test loss'; Table 4), the discriminant analysis model performed best (test loss = 0.06) and correctly classified 97% of the erosion objects (200 of 207; equivalent to 94% of the erosion volume) and 88% of the vegetation objects (78 of 89). The most important predictors (determined with automated feature selection in MATLAB) were NDVI, aspect, elevation change, and elevation in 2009–2011.

Table 4
Performance of the machine learning algorithms in classifying negative and positive change objects.

Algorithm	Negative change test loss	Positive change test loss
k-nearest neighbors	0.10 ($k = 3$)	0.24 ($k = 11$)
decision trees	0.08	0.20
naïve Bayes	0.09	0.19
discriminant analysis	0.06	0.17
support vector machines	0.09	0.21

3.2.3. Deposition

Positive change classification into 'deposition', 'vegetation', and 'other objects' for changes related to construction, etc. used a similar procedure to negative change classification with two additional predictors (Table 3). The test loss varied between 0.17 and 0.24 for the five tested machine learning algorithms (Table 4). As with negative changes, discriminant analysis performed best (test loss = 0.17), correctly classifying 91% of vegetation objects (161 of 177), 77% of other objects (83 of 108), and 60% of deposition objects (9 of 15; equivalent to 95% deposition volume). The most important predictors (determined with automated feature selection in MATLAB) were NDVI, aspect, elevation change, and slope.

3.2.4. Model application on full inventories

We ran the discriminant analysis models on the full object inventories using all predictors because using only the most important predictor subset increased test loss to 0.08 (erosion) and 0.19 (deposition). Results were checked visually and edited manually if needed. Lastly, adjacent erosion and deposition objects that were previously treated separately because of the NDVI thresholding (Fig. 5) were re-merged, resulting in a final inventory of cliff change objects.

3.3. Erosion metrics and characteristics

The change object inventory was used to assess erosion object characteristics and distributions, and to quantify regional changes. The relationship between erosion object area, *A*, and volume, *V*, was represented as:

Table 3
Predictors used to classify change objects within coastal cliff faces. Asterisks (*) indicate predictors that are calculated from the 2009–2011 topography for the negative change and from the 2016 topography for the positive change. Predictors #12–13 are only used for the positive change.

#	Predictor	Unit	Metrics (if > 1)	Meaning/comments	ArcMap tool
1	Distance from the cliff base	m		Shortest planar distance between object edge and the cliff base line	*Near*
2	Distance from the cliff top	m		Shortest planar distance between object edge and the 2009–2011 cliff top line	*Near*
3	Area	m^2		Planar area of object	*Calculate Geometry Attributes*
4	Elevation 2009–2011	m NAVD88	Min, max, range, mean, std. dev		*Zonal Statistics as Table*
5	Elevation 2016	m NAVD88	Min, max, range, mean, std. dev		*Zonal Statistics as Table*
6	Elevation change	m	Min, max, range, mean, std. dev, sum	Change raster values Sum × 1 m^2 equals total object volume	*Minus; Zonal Statistics as Table*
7	Slope*	degrees	Min, max, range, mean, std. dev	Maximum rate of change in DEM value in 3 × 3 cell neighborhood	*Slope; Zonal Statistics as Table*
8	Roughness*	degrees	Min, max, range, mean, std. dev	Standard deviation of slope in 5 × 5 cell neighborhood	*Focal Statistics; Zonal Statistics as Table*
9	Aspect*	degrees	Range, std. dev	Downslope direction of the maximum rate of DEM change in 3 × 3 cell neighborhood	*Aspect; Zonal Statistics as Table*
10	NDVI*	n/a	Min, max, mean		*Zonal Statistics as Table*
11	Width to length ratio	$m\ m^{-1}$		Minimum bounding rectangle width divided by length	*Minimum Bounding Geometry*
12	Distance to erosion	m		Positive change only; shortest planar distance between object edge and the nearest erosion object	*Near*
13	Direction of erosion	degrees		Positive change only; difference in the angle between positive object to the nearest point along the cliff top 2009–2011, and the positive object to the nearest erosion object (range 0–180°)	*Near*

$$V = a\,A^{b} \quad (1)$$

where a is a constant and b is the power-law exponent, whose value may be indicative of underlying mechanisms. Higher b values (>1.3) are typical for inventories with relatively deep landslides, while lower values are more typical for inventories of near-surface detachments (Larsen et al., 2010). Assessing the degree of fit to the power-law (Eq. (1)) allows the identification of scale-invariant behavior (close fit), or alternatively, a change in mechanism as a function of volume (Guzzetti et al., 2009; Swirad et al., 2019). The relationship between erosion object volume, V, and the non-cumulative frequency of occurrence, $f(V)$, was represented as:

$$f(V) = \alpha\,V^{-\beta} \quad (2)$$

where α is a constant and β is the power-law exponent, with higher values indicating a larger proportion of smaller objects in the inventory (Malamud et al., 2004) and potentially discontinuous rock faces, as opposed to more homogeneous rock (Hungr et al., 1999).

Regional change metrics were calculated at the state and county levels. They include: total eroded and deposited volumes, net erosion (eroded volume – deposited volume), net erosion rate per meter of coastline (net erosion/coastline length/timespan), and net cliff retreat rate (net erosion/coastline length/average cliff height/timespan). Additionally, we explored cliff face erosion rates in 10 km alongshore blocks. The timespan was calculated using the last survey of the 2009–2011 LiDAR dataset for each of the 22 alongshore survey blocks (Table 1) and April–May 2016, and was averaged over the coastal reach investigated.

4. Results

4.1. Cliff mapping and object detection

Cliffs were automatically mapped along 1011 km of the California coastline. Removal of areas with insufficient topographic data quality resulted in 866 km of coastline (~52% of the California coastline and ~ 86% of mapped California cliffs) and 4.96×10^7 m^2 of cliff face surfaces for analysis. The alongshore-averaged cliff base and top elevations were 2.4 m and 44.5 m NAVD88, respectively, resulting in an average cliff height of ~42 m. The mean cliff slope was 40° (max 82°).

The modelling alone (before visual inspection) suggested that 1.51×10^7 m^3 material was eroded and 1.22×10^6 m^3 deposited (Table 5). Manual editing decreased automatically classified erosion and deposition volumes by 11% and 20%, respectively. After re-merging adjacent objects (previously split by vegetation surface conditions, Fig. 5) the final inventory consisted of 45,699 erosion objects with a total volume of 1.34×10^7 m^3, and 1728 deposition objects with a total volume of 9.72×10^5 m^3 (Table 5).

Table 5
Summary of results using machine learning and manual editing to classify coastal cliff change into objects.

Change type	Number of objects	Total change volume (m^3)
a) Negative change		
Change objects detected using thresholds	94,130	1.79×10^7
Change objects classified as 'erosion' by machine learning	65,521	1.51×10^7
Erosion objects after manual editing	51,438	1.34×10^7
Erosion objects after re-merging adjacent objects	45,699	1.34×10^7
b) Positive change		
Change objects detected using thresholds	52,862	6.57×10^6
Change objects classified as 'deposition' by machine learning	2266	1.22×10^6
Deposition objects after manual editing	4017	9.72×10^5
Deposition objects after re-merging adjacent objects	1728	9.72×10^5

4.2. Coastal cliff erosion and deposition characteristics

The number of erosion objects was 26 times larger than deposition objects, indicating deposit residence time was <~7 years for most failure events. Erosion objects ranged in area from 10 m^2 (imposed minimal footprint) to 1.12×10^5 m^2, and in volume from 6.43 m^3 to 7.52×10^5 m^3. Deposition objects ranged in area from 10 m^2 to 1.45×10^4 m^2, and in volume from 6.89 m^3 to 9.86×10^4 m^3. About 10% of the cliff face experienced erosion from 2009−2011 to 2016, and ~ 1% was covered in landslide deposits in 2016, considering the detection limits. Net erosion was 1.24×10^7 m^3, equivalent to cliff-averaged vertical change of −0.25 m, and net cliff face retreat of 0.34 m (assuming a mean cliff height of 42 m along 866 km of cliffs, Table 6). The net erosion rate was 2.14×10^6 m^3 yr^{-1} over the whole study area, equivalent to 2.47 m^3 yr^{-1} per meter of coastline.

A strong correlation ($r^2 = 0.92$, $p < 0.05$) exists between the area and volume of erosion objects with a b exponent of 1.13 (Eq. (1), Fig. 6a). The non-cumulative volume-frequency distribution tightly fits to the power-law ($r^2 = 0.99$, $p < 0.05$) for objects between ~14 m^3 and 1.45×10^5 m^3 with the power-law exponent β of 0.80 (Eq. (2)). We observe a rollover (a relatively lower number of objects) for small (<~14 m^3) and large (>1.45×10^5 m^3) volume objects (Fig. 6b). Erosion objects smaller than 14, 25, and 60 m^3 comprise 25%, 50%, and 75% of the erosion object inventory, respectively. Erosion objects larger than 3243 m^3 constitute 1% of the inventory and 67% of the total eroded volume (Fig. 6c).

The number and sizes of erosion objects varied between regions and counties, with generally higher erosion rates and larger erosion objects in northern California compared to southern California. The highest number of erosion objects normalized by the coastline length occurred in Sonoma County (Table 7). Humboldt County experienced the most erosion, the largest mean erosion object volume, and the inventory with highest proportion of large objects (described by the lowest β). Average cliff retreat rates ranged from 0.003 m yr^{-1} in Orange County to 0.18 m yr^{-1} in Humboldt County (Table 7).

Retreat rates for the 10 km alongshore blocks ($n = 137$) averaged 0.07 ± 0.12 m yr^{-1} (std dev) and ranged from 0 to 1.16 m yr^{-1}. The highest retreat rates (>0.2 m yr^{-1}; 6% blocks) were observed in San Mateo (0.3 m yr^{-1}), Marin (0.3 m yr^{-1}), and Humboldt (1.16 m yr^{-1}) Counties. 58% of blocks were characterized by relatively low retreat rates <0.05 m yr^{-1} (Fig. 7b).

Table 6
Summary of the erosion and deposition within California coastal cliffs between 2009−2011 and 2016.

Cliff change metric	Erosion	Deposition
Number of objects	45,699	1728
Total area (m^2)	4.84×10^6	3.97×10^5
Proportion of cliff face (%)	9.8	0.8
Mean object area (m^2)	106	230
Standard deviation of area (m^2)	1084	680
Largest object area (m^2)	1.12×10^5	1.45×10^4
Smallest object area (m^2)	10	10
Mean object volume (m^3)	293	562
Standard deviation of volume (m^3)	5324	3172
Largest object volume (m^3)	7.52×10^5	9.86×10^4
Smallest object volume (m^3)	6.43	6.89
Total volume (m^3)	1.34×10^7	9.72×10^5
Average elevation change (m)	−2.76	2.45
Net erosion (m^3)	1.24×10^7	
Net cliff-averaged elevation change (m)	−0.25	
Net erosion rate (m^3 yr^{-1})	2.14×10^6	
Net erosion rate per meter of coastline (m^3 yr^{-1})	2.47	
Net cliff retreat rate (m yr^{-1})	0.06	

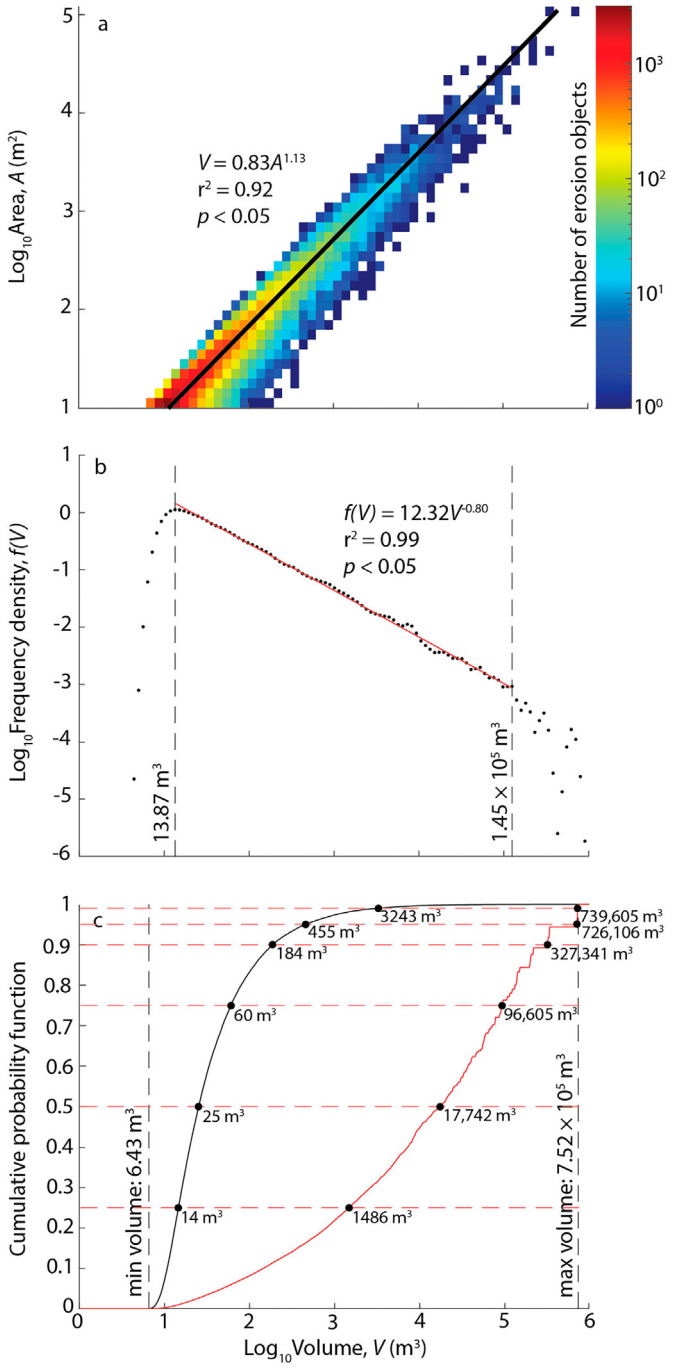

Fig. 6. Size distribution of erosion objects identified for California coastal cliffs between 2009−2011 and 2016: a) the relationship between erosion area and volume and fitted power-law trendline (black line); b) non-cumulative volume-frequency distribution of erosion objects and the power-law trendline (red line) fitted for volumes between ~14 m^3 and 1.45 × 10^5 m^3 marked by the vertical dashed lines; c) cumulative distribution (0.01 $\log_{10}$ bin width) of number of erosion objects (black line) and total eroded volume (red line); horizontal dashed lines represent 25th, 50th, 75th, 90th, 95th and 99th percentile; vertical dashed lines represent the smallest and the largest object.

5. Discussion

This study builds upon previous work to quantify California cliff erosion over large spatial scales at high resolution (Hapke et al., 2009; Young, 2018) by including automated procedures to delineate the cliff face and applying machine learning methods to classify change objects. The improved automated workflow reduces manual digitizing, editing,

Table 7
Summary of coastal cliff erosion between 2009−2011 and 2016 for California counties.

County	Alongshore extent (km)	Mapped cliff length (km)	Inspected cliff length (km)	Inspected cliff face area (m^2)	Mean cliff height (m)	Analysis timespan (yr)	Number of erosion objects	Total eroded volume (m^3)	Mean erosion object volume (m^3)	Volume-frequency β	Number of deposition objects	Total deposition volume (m^3)	Net erosion (m^3)	Net erosion rate per meter of coastline (m^3 yr^{-1} m^{-1})	Average cliff face retreat rate (m yr^{-1})	
															2009–2011 to 2016	1998 to 2009–2011 (Young, 2018)
Del Norte	1576-1646	39	21	1.74×10^6	68	4.9	737	4.08×10^5	554	0.77	96	2.76×10^4	3.81×10^5	3.76	0.05	
Humboldt	1382-1576	90	69	8.95×10^6	80	4.8	2742	4.60×10^6	1676	0.64	336	2.26×10^5	4.37×10^6	13.12	0.18	
Mendocino	1209-1382	146	128	9.22×10^6	60	5.0	7427	1.90×10^6	255	0.91	378	3.05×10^5	1.59×10^6	2.49	0.05	
Sonoma	1126-1209	71	48	2.89×10^6	36	5.5	5110	4.54×10^5	89	1.11	40	7479	4.46×10^5	1.67	0.05	0.01
Marin	1015-1126	76	52	4.19×10^6	63	5.6	3448	1.36×10^6	394	0.78	231	1.08×10^5	1.25×10^6	4.34	0.09	0.07
San Francisco	996-1015	7	5	3.27×10^5	42	5.6	209	9.02×10^4	432	0.72	17	952	8.92×10^4	3.34	0.16	0.16
San Mateo	915-996	69	62	2.80×10^6	31	5.6	2436	1.28×10^6	526	0.74	107	6.65×10^4	1.21×10^6	3.53	0.12	0.09
Santa Cruz	853-915	48	48	1.23×10^6	24	5.6	1483	1.66×10^5	112	1.27	10	853	1.65×10^5	0.61	0.03	0.04
Monterey	686-853	123	116	7.26×10^6	48	5.8	9474	8.85×10^5	93	1.3	243	9.44×10^4	7.85×10^5	1.16	0.02	0.01
San Luis Obispo	546-686	92	88	2.67×10^6	21	6.2	3847	2.50×10^5	65	1.18	46	1.02×10^4	2.46×10^5	0.45	0.03	0.04
Santa Barbara	370-546	131	119	3.90×10^6	25	6.5	4964	1.13×10^6	227	0.97	112	2.67×10^4	1.10×10^6	1.41	0.07	0.05
Ventura	303-370	1	1	4.75×10^4	19	6.5	72	8204	114	0.88	0	0	8206	0.91	0.06	0
Los Angeles	187-303	36	35	2.03×10^6	38	6.6	1388	5.79×10^5	417	0.94	80	9.25×10^4	4.87×10^5	2.13	0.05	0.02
Orange	120-187	17	16	4.60×10^5	20	6.6	233	7248	31	1.92	0	0	7248	0.07	0.003	0.01
San Diego	0-120	64	57	2.19×10^6	25	6.6	2129	2.74×10^5	129	0.96	32	5027	2.69×10^5	0.72	0.03	0.02
All counties	0-1646	1011	866	4.96×10^7	42	5.8	45,699	1.34×10^7	293	0.8	1728	9.72×10^5	1.24×10^7	2.47	0.06	0.04

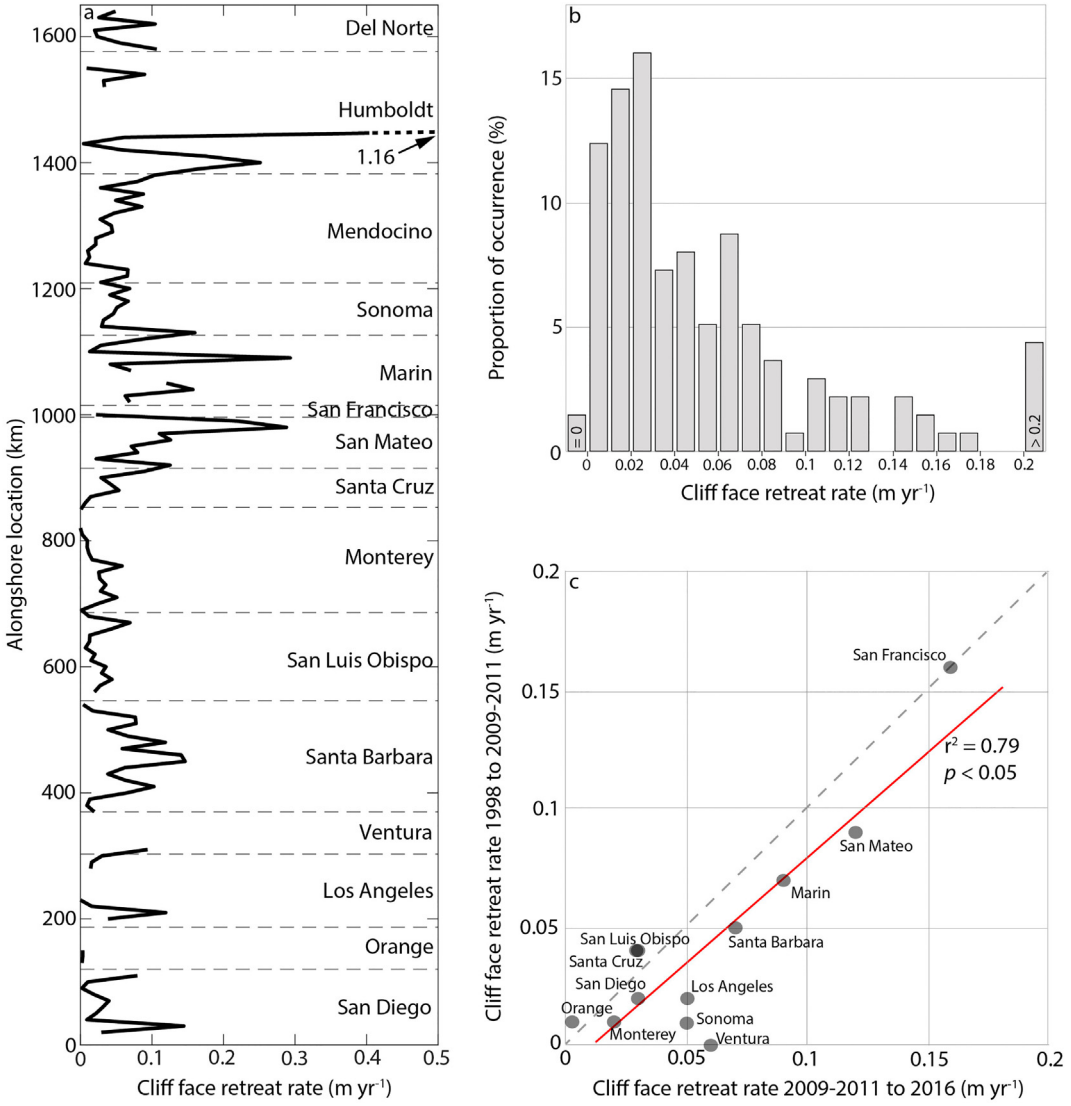

Fig. 7. Coastal cliff face retreat rates in California between 2009−2011 and 2016: a) rates averaged over 10 km alongshore blocks where 0 km represents the USA/Mexico border and 1646 km represents the California/Oregon border; dashed lines delimit counties; b) relative occurrence of retreat rates (for all 10 km blocks from [a]) in 0.01 m yr^{-1} bins; c) relationship between county-averaged changes between 2009−2011 to 2016 and 1998 to 2009–2011 (Young, 2018) cliff face retreat rates; red line represents the best-fit linear regression and dashed line is the 1:1 relationship.

classification, and processing time, allowing efficient quantification of coastal cliff erosion.

5.1. Data quality and limitations

The 2.5D change detection methods presented here provide consistency by eliminating resolution differences in point cloud density between the surveys. Limitations of the 2.5D method, when used from a top view, include the inability to model and measure erosion of oververtical (or over-hanging) surfaces such as sea caves and notches (Young et al., 2010a; Cook, 2017). While these features are locally important for cliff stability analysis, they are relatively limited along the California coast, and unlikely to significantly impact the overall erosion volume results. Change detection performed directly on point clouds explored elsewhere (e.g. Benjamin et al., 2016; Cook, 2017) could be considered for future surveys with consistent quality and point density.

Datum differences between the two surveys used here were relatively small (~2 cm; Martin, 2012) compared to survey accuracy, and were implicitly addressed by using detection thresholds and masking out cliffs that contained erroneous change data. Future studies could be improved by including methods to decrease potential spatial offset, such as tight point cloud co-registration before converting into DEMs (Abellán et al., 2010), iterative shifting of DEMs over *n* pixel window (Nuth and Kääb, 2011) or, in cases of tectonically active areas, removal of the geoid correction from a pre-event DEM and elevation subtraction from a smoothed post-event DEM (Oskin et al., 2012).

Statistically derived levels of detection such as used here (1.96 × RMSZ at 95% confidence level) are preferred for reliable change detection and suppressing noise (Höhle and Höhle, 2009). An alternative approximation could be the 99.9% quantile of noise distribution (Dewez et al., 2013). We applied a uniform vertical level of detection because of differences in survey quality and high topographic complexity. However, where a range of cliff forms are present, using a non-uniform threshold could help detection in areas such as low magnitude change on flatter surfaces (Wheaton et al., 2010). If subsequent LiDAR surveys maintain the quality of the 2016 dataset, RMSZ is likely to decrease allowing a smaller vertical level of detection.

The minimal surface footprint of ten connected cells was optimized based on analysis of unchanging control areas, as a threshold above which no erroneous change was detected. While change detection with smaller thresholds is possible, we opted for larger threshold levels

in return for less error. In result, the overall methods produced conservative erosion estimates because small volume objects were neglected.

Masking out cliff faces with insufficient data, survey errors, and geodetic offset between the two surveys limited analysis to <80% of mapped cliff faces in San Francisco, Marin, Sonoma, Humboldt, and Del Norte Counties (Table 7). As a result, identified characteristics of erosion may not fully represent changes occurring on coastal cliffs in these entire counties. Future survey efforts could target areas in northern California that still lack high-quality repetitive LiDAR surveys.

5.2. Cliff base and top detection

Parameter values used to identify cliff base and top positions reflect local conditions. For instance, typical cliff base elevations in California are between 0 and 4 m NAVD88, while cliff top elevations are usually in the range of 15–100 m NAVD88. The seaward and landward slope angles for 10 consecutive points at 1 m intervals were optimum here, because most California cliffs extend >10 m cross-shore. Optimal parameters may vary for other study locations and should be tested. Future efforts for cliff base and top detection could use alternative methods, such as machine learning, potentially further reducing manual editing. Other possible improvements could include a region-growing approach for cliff zone identification.

Cliff base detection was less successful where meter-scale steps or low slope landslide deposits were present at the cliff base. Generally, the cliff top was correctly identified for cliffs cut into uplifted marine terraces, where the cliff top slope break is often distinct. However, complex lithology and structure of the California coast results in a range of cliff face cross-sections (Griggs et al., 2005), and cliff top detection was less successful for areas where within-cliff flattening exists and for cliff sections with high alongshore variability. Building edges sometimes mapped as cliff tops (Fig. 3a) could be eliminated in future studies by masking infrastructure. Overall, using numerical thresholds improved objectivity, consistency, and efficiency and only 10% of cliff base and 29% of cliff top locations required manual editing.

Some sections of the coast (e.g. Big Sur, Point Sal, King Range) contain mountain slopes, and separating cliff faces from hinterland is challenging because of subtle slope changes. At these locations, coastal and hillslope systems are likely connected, and landslides such as Mud Creek (Warrick et al., 2019) can encompass both the cliff face and the hillslope behind it. This study explicitly focused on the coastal cliff, but the hillslope-level processes should be considered for decision making and land management, as hinterland slopes may be unstable even if not directly influenced by wave action. For example, we identified 131 landslides just outside the analysis zone used in this study (e.g. Fig. 8c).

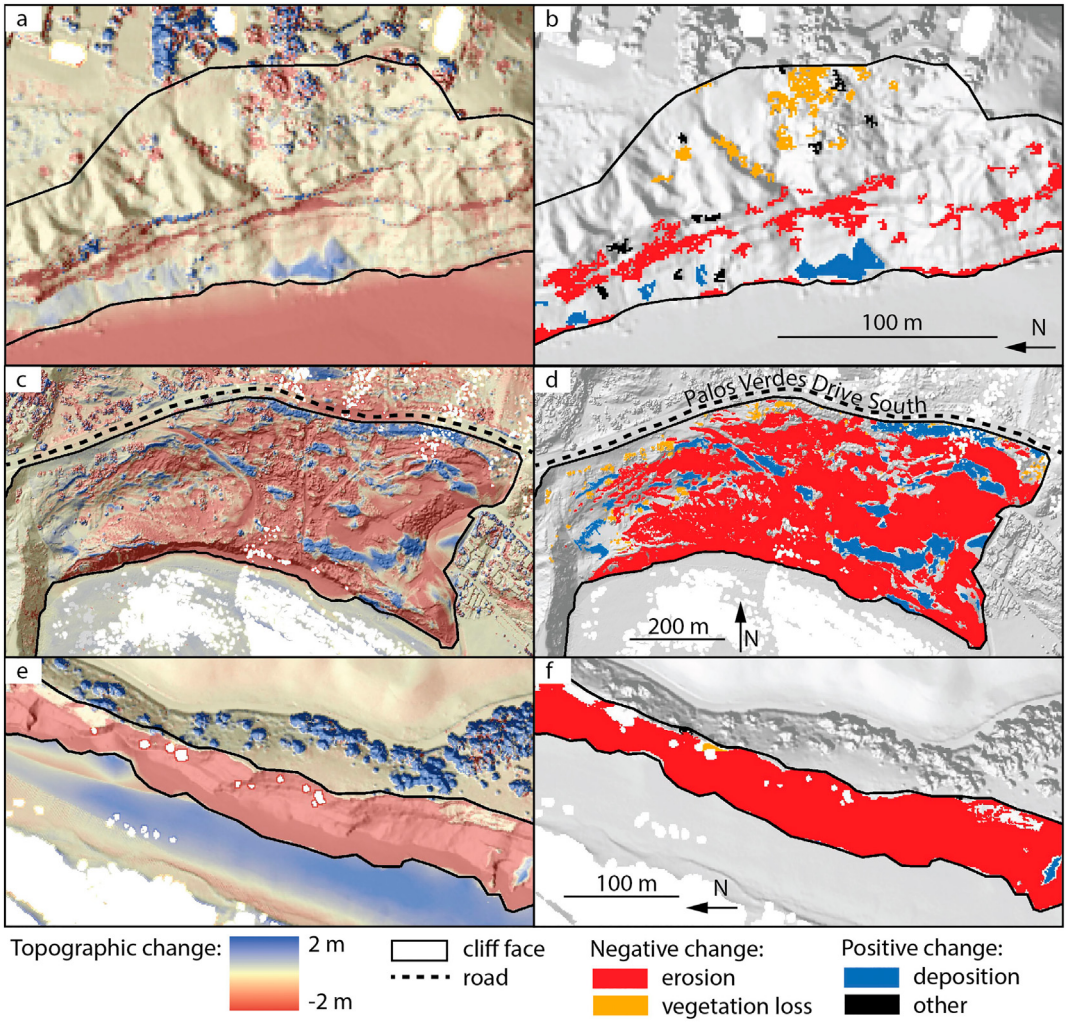

Fig. 8. Examples of detected change: a-b) smaller-scale rockfalls on the near-vertical cliff face (red), with deposition at the cliff base (blue) and vegetation change on the upper cliff section (yellow), Torrey Pines, San Diego; c-d) deep-seated landslide, Portuguese Bend, Palos Verdes; e-f) erosion of the entire cliff face, Centerville Beach, Ferndale. Change rasters are saturated at −2 and 2 m vertical change (left panels).

5.3. Object classification

Discriminant analysis was the most successful classification algorithm, potentially because it is less dependent on the training data noise compared to other algorithms, and does not assume predictor independence (Alpaydin, 2014). Therefore, discriminant analysis likely outperformed other algorithms because of the heterogeneity of California cliffs, including the range of mass movement types and sizes, and vegetation surface conditions.

The most important predictors were NDVI, variability in aspect, elevation and the magnitude of change. The NDVI optical signature captures differences in reflectance spectra signatures between bare and vegetated surfaces, particularly in the near-infrared range (Bowker et al., 1985). However, in this study, the NDVI value alone was not sufficient to clearly separate mass movements from vegetation, possibly because of: 1) distortions of the spectral imagery (Maxwell et al., 2014; Ma et al., 2017); 2) cliff failures that include vegetated cliff sections; and 3) temporal offsets between topographic (2009–2011 LiDAR) and optical (2009 NAIP) surveys (if vegetation changes occurred between these two surveys). Vegetation objects are characterized by diverse aspects (orientation) resulting from their complex structures. Conversely, the direction that cliffs face influences erosion object orientation, resulting in more consistent aspects of erosion objects compared to vegetation. Dense vegetation is limited near the shoreline and smaller objects (<~20 m^3) located near the cliff base and at lower elevations are usually mass movements (Fig. 8a-b). Predictors related to the magnitude of change also help separate erosion from vegetation change (Fig. 8c-d). For example, large (≥1000 m^3) change objects mostly represent erosion, while vegetation change objects often have more variable vertical change (high range and standard deviation of change raster values) as compared to erosion objects.

Using a larger known-class inventory, particularly for deposition objects, could improve model performance, allowing the algorithm to more accurately capture feature characteristics compared to other changes. Automated deposition detection could also be improved by using stratified sampling to balance classes in the training set, and by developing location metrics that consider topographic influence on mass movement direction rather than the planform proximity and relative angle to erosion objects.

5.4. Implications for rock coast studies

Data-driven analyses at large scale (>100 km) allow detection of regional change patterns impossible to constrain when inspecting short sections of a coastline. This study contributes to limited literature that investigates large-area cliff face erosion.

5.4.1. Erosion rates

Converting Schmidt hammer rebound values (Young, 2018) to uniaxial compressive strength using the Katz et al. (2000) model yields an average of 23 ± 29 (std dev) MPa, typical for weak (0–25 MPa) and medium hardness (25–50 MPa) rock classes (Prémaillon et al., 2018). Retreat rates calculated here are generally consistent with global retreat rates for weak and medium hardness rocks (Prémaillon et al., 2018) and Tertiary sedimentary rocks and shales (Woodroffe, 2002).

5.4.2. Spatial patterns

Alongshore variability in cliff face retreat rates at county and 10 km scales could be related to several possible drivers. First, both annual rainfall and erosion generally increase northwards, consistent with rain induced landsliding mechanisms (e.g. Reichenbach et al., 2018). However, Stanley et al. (2020) suggested using rainfall metrics that are relative to the decadal-scale average. Second, offshore significant wave height is larger in central and northern California compared to southern California (Fig. 1), which may increase wave-driven erosion. However, other factors such as beach sand levels, tides, wave runup, etc. also influence wave processes (Young et al., 2016, 2021). Third, this study encompassed the 2015–2016 El Niño event, and in some areas the 2009–2010 El Niño event (Table 1), which had variable impacts along the California coast. For example, the 2015–2016 event is one of the strongest El Niños on record, causing widespread beach erosion (Barnard et al., 2017), yet Young et al. (2018) observed lower than average cliff erosion rates in southern California which they ascribed to low rainfall, a northerly swell approach, and asynchronous large swells and high tides. Fourth, erosion resistance, controlled by lithology and structure (Sunamura, 1992), varies alongshore (Hapke et al., 2014). Lastly, cliff armoring, prevalent in southern California, locally limits erosion (e.g. Young, 2018).

5.4.3. Temporal patterns

The state-averaged cliff face retreat rate of 0.06 m yr^{-1} is the same order of magnitude measured between 1998 and 2009–2011 for southern and central California (0.04 m yr^{-1}, Young, 2018). The difference between the two epochs is potentially from inclusion of faster eroding cliffs of northern California in the present inventory, differences in detection thresholds, the stochastic nature of cliff erosion, and/or time-varying environmental conditions such as El Niño. At a county level, cliff face retreat rates in the two epochs were correlated ($r^2 = 0.79$, $p < 0.05$) with slightly higher rates in the more recent period (Fig. 7c). This differs from Young (2018) who observed that at much finer resolution (5 m alongshore), historical (1920s–1930s to 1998) and more recent (1998 to 2009–2011) cliff top retreat rates were significantly inversely correlated for areas with large retreat rates in either epoch. Further analyses are needed to examine the differences between retreat histories and cyclic erosion patterns at local (m) and regional (km) scales over varying time periods.

5.4.4. Detachment sizes

We found an area-volume exponent b of 1.13 (Eq. (1); Fig. 6a), which is characteristic of relatively shallow landslide inventories (Larsen et al., 2010). However, we observed many deep-seated landslides in the dataset, and the order of magnitude volume range characterizing any given footprint size suggests a range of possible erosion mechanisms (Swirad et al., 2019), consistent with the wide range of geological and geomorphological settings in California (Griggs et al., 2005; Hapke et al., 2014). The observed volume-frequency exponent β of 0.80 (Eq. (2); Fig. 6b) is within the typical range (0.4–1.1) for mass movements (Santana et al., 2012). The relatively high β characterizing Orange County erosion features suggests more smaller, shallower erosion events, while the low β characterizing erosion in Humboldt and Del Norte Counties suggests a higher relative proportion of larger, deeper landslides, or event superposition (Table 7). The volume-frequency rollover observed for the smallest (<~14 m^3) objects could be caused by limited detection of small objects (from georeferencing errors, vertical accuracy and the detection thresholds used; Olsen et al., 2015), superposition of smaller events, misclassification of smaller erosion objects, and/or limits on the erosion size imposed by rock structure (Hungr et al., 1999; Malamud et al., 2004). More research is needed to validate the power-law relationship for smaller erosion features (<~14 m^3) and over shorter timescales (Williams et al., 2018, 2019; Young et al., 2021). Objects larger than 1.45×10^5 m^3 were less frequent than predicted with the power-law relationship (Fig. 6b) and may indicate a cliff height influence on the maximum landslide size (Fig. 8e). Overall, the size and area-volume distributions suggest that our erosion inventory generally includes small to medium-scale cliff failures (Fig. 8a-b), catastrophic events (Fig. 8c-d), and sections where the entire cliff face retreated, shifting the coastline inland (Fig. 8e-f). Detailed geological and geomorphologic analysis could reveal the mechanism of mass movement through sliding, collapse, etc.

5.4.5. Sediment budget

The key variables in estimating the coastal cliff beach-sediment contribution include the rate of cliff erosion and the amount of coarse-grained sediment within the cliffs that will potentially remain in the nearshore littoral system. After a cliff failure, wave action disaggregates the failed material and mobilizes the fine-grained sediments, which are transported offshore. In contrast, coarse sediments are typically retained in the littoral zone and supply new beach-building material. The grain size threshold nominally separating these depositional environments is known as the littoral cutoff diameter (Hicks and Inman, 1987; Best and Griggs, 1991; Limber et al., 2008). The relative importance of cliffs as natural sand sources varies widely across California and depends on the spatial extent and time period being analyzed (e.g. Flick, 1993; Patsch and Griggs, 2006, 2008; Young and Ashford, 2006; Young et al., 2010b). The average erosion rate measured from 2009–2011 to 2016 was 2.47 $m^3\ yr^{-1}$ per meter of coastline with a maximum of >13 $m^3\ yr^{-1}$ in Humboldt County. These results provide an opportunity to refine statewide estimates of cliff sediment contributions to the California coast, however more research is needed to determine the percent of coarse grain cliff material in many areas.

6. Conclusions

This study quantified cliff erosion along 866 km of California coastline between 2009–2011 and 2016 using airborne LiDAR DEMs. The workflow automates cliff face delineation and change object classification, greatly reducing processing time and subjectivity. Change detection and object classification combined 2.5D DEM analysis, vertical and areal detection thresholds, spectral surface signatures (NDVI), machine learning methods, and manual quality control. Machine learning object classification methods separated erosion and deposition from other changes within the cliff face, notably the loss and growth of vegetation. Five algorithms were trained and tested on two sets of 1000 manually labelled change objects. Discriminant analysis performed best, with test losses of 0.06 and 0.17, for negative and positive change object classification, respectively. Visual inspection and manual editing of the automated object classification reduced the final calculated erosion and deposition volumes by 11% and 20%, respectively.

Overall, 10% of California cliff faces studied experienced erosion and 1% retained new deposits of eroded material. Net cliff erosion was $1.24 \times 10^7\ m^3$, equal to the net erosion rate of 2.47 $m^3\ yr^{-1}$ per meter of coastline, and average cliff retreat rate of 0.06 m yr^{-1}. Erosion objects varied in size from 6.43 m^3 to $7.52 \times 10^5\ m^3$. Erosion object area and volume were strongly correlated ($r^2 = 0.92$). The volume-frequency relationship fit a power law for volumes ranging from ~14 m^3 to $1.45 \times 10^5\ m^3$ with an exponent of $\beta = 0.80$, typical for terrestrial mass movements. The largest 1% of erosion objects (>3243 m^3) comprised 67% of the total eroded volume. Humboldt County experienced the highest cliff retreat rate (0.18 m yr^{-1}), while cliff erosion in Orange County was relatively limited (0.003 m yr^{-1}). The analysis of large-scale LiDAR datasets, facilitated by automated methods, can help inform regional decision making and coastal change modelling. With calibration, the methods are generally applicable to other cliffed coastlines.

Declaration of competing interest

The authors declare that they have no known competing financial interests or personal relationships that could have appeared to influence the work reported in this paper.

Acknowledgments

We are grateful for primary funding provided by the California Ocean Protection Council (C0303100) administered by University of Southern California Sea Grant. Additional support was provided by the California Department of Parks and Recreation, Natural Resources Division Oceanography Program (C1670004 and C19E0049). We acknowledge freely-available LiDAR datasets hosted by the NOAA Office for Coastal Management (coast.noaa.gov), imagery of National Agriculture Imagery Program available via California State Geoportal (gis.data.ca.gov), historical coastline layer of California Department of Fish and Wildlife (purl.stanford.edu/hj484bt5758), paved road layer by OpenStreetMap community (www.openstreetmap.org), the wave and tidal information by NOAA (ndbc.noaa.gov; tidesandcurrents.noaa.gov), the rainfall information by Western Regional Climatic Center (wrcc.dri.edu) and the airborne photographs by Kenneth and Gabrielle Adelman of California Coastal Record Project (Californiacoastline.org). We thank Jessica Carilli for manuscript proofreading and three anonymous reviewers for providing insightful comments.

Appendix A. Supplementary data

Supplementary data to this article can be found online at https://doi.org/10.1016/j.geomorph.2021.107799.

References

Abellán, A., Calvet, J., Vilaplana, J.M., Blanchard, J., 2010. Detection and spatial prediction of rockfalls by means of terrestrial laser scanner monitoring. Geomorphology 119, 162–171.
Alpaydin, E., 2014. Introduction to Machine Learning. 3rd edition. MIT Press, Cambridge, MA, USA.
Amatya, P., Kirschbaum, D., Stanley, T., 2019. Use of very high-resolution optical data for landslide mapping and susceptibility analysis along the Karnali Highway, Nepal. Remote Sens. 11, 2284.
Ashton, A.D., Walkden, M.J., Dickson, M.E., 2011. Equilibrium responses of cliffed coasts to changes in the rate of sea level rise. Mar. Geol. 284 (1), 217–229.
Barnard, P.L., Hoover, D., Hubbard, D.M., Snyder, A., Ludka, B.C., Allan, J., Kaminsky, G.M., Ruggiero, P., Gallien, T.W., Gabel, L., Diana McCandless, D., Weiner, H.M., Cohn, N., Anderson, D.L., Serafin, K.A., 2017. Extreme oceanographic forcing and coastal response due to the 2015–2016 El Niño. Nat. Commun. 8, 14365.
Benjamin, J., Rosser, N.J., Brain, M.J., 2016. Rockfall detection and volumetric characterisation using LiDAR. In: Aversa, et al. (Eds.), Landslides and Engineered Slopes. Experience, Theory and Practice. Associazione Geotecnica Italiana, Rome, Italy.
Benjamin, J., Rosser, N.J., Brain, M.J., 2020. Emergent characteristics of rockfall inventories captured at a regional scale. Earth Surf. Process. Landf. 45, 2773–2787.
Best, T.C., Griggs, G.B., 1991. A sediment budget for the Santa Cruz littoral cell. Society of Economic Paleontologists and Mineralogists SP46, pp. 35–50.
Blaschke, T., 2010. Object based image analysis for remote sensing. ISPRS J. Photogramm. Remote Sens. 65, 2–16.
Bowker, D.E., Davis, R.E., Myrick, D.L., Stacy, K., Jones, W.T., 1985. Spectral reflectances of natural targets for use in remote sensing studies. NASA Reference Publication. 1139 . https://ntrs.nasa.gov/citations/19850022138.
Brooks, S.M., Spencer, T., 2010. Temporal and spatial variations in recession rates and sediment release from soft rock cliffs, Suffolk coast, UK. Geomorphology 124 (1–2), 26–41.
Clark, A.R., Lee, E.M., 2002. Investigation and Management of Soft Rock Cliffs. Thomas Telford, London.
Collins, B.D., Sitar, N., 2008. Processes of coastal bluff erosion in weakly lithified sands, Pacifica, California, USA. Geomorphology 97, 483–501.
Cook, K.L., 2017. An evaluation of the effectiveness of low-cost UAVs and structure from motion for geomorphic change detection. Geomorphology 278, 195–208.
Dewberry, 2012. LiDAR Quality Assurance (QA) Report California LiDAR and Imagery QA NOAA Coastal Services Center. Tampa, FL, USA.
Dewberry, 2016. 2016 West Coast El Nino 2016 B16 LiDAR. Report Produced for U.S. Geological Survey, Tampa, FL, USA.
Dewez, T.J.B., Rohmer, J., Regard, V., Cnudde, C., 2013. Probabilistic coastal cliff collapse hazard from repeated terrestrial laser surveys: case study from Mesnil Val (Normandy, northern France). J. Coast. Res. SI65, 702–707.
Dickson, M.E., Perry, G.L.W., 2016. Identifying the controls on coastal cliff landslides using machine-learning approaches. Environ. Model. Softw. 76, 117–127.
Earlie, C.S., Masselink, G., Russell, P.L., Shail, R.K., 2015. Application of airborne LiDAR to investigate rates of recession in rocky coast environments. J. Coast. Conserv. 19, 831–845.
Emery, K.O., Kuhn, G.G., 1980. Erosion of rock shores at La Jolla, CA. Mar. Geol. 37, 197–208.
Emery, K.O., Kuhn, G.G., 1982. Sea cliffs: their processes, profiles, and classification. Geol. Soc. Am. Bull. 93 (7), 644–654.
Flick, R.E., 1993. The myth and reality of Southern California beaches. Shore & Beach 3–13.
Ghorbanzadeh, O., Blaschke, T., Gholamnia, K., Meena, S.R., Tiede, D., Aryal, J., 2019. Evaluation of different machine learning methods and deep-learning convolutional neural networks for landslide detection. Remote Sens. 11, 196.
Goetz, J.N., Brenning, A., Petschko, H., Leopold, P., 2015. Evaluating machine learning and statistical prediction techniques for landslide susceptibility modeling. Comput. Geosci. 81, 1–11.

Griggs, G., Patsch, K., Savoy, L., 2005. Living with the Changing California Coast. University of California Press, Berkeley, CA, USA.
Guzzetti, F., Ardizzone, F., Cardinali, M., Rossi, M., Valigi, D., 2009. Landslide volumes and landslide mobilization rates in Umbria, central Italy. Earth Planet. Sci. Lett. 279 (3), 222–229.
Hapke, C.J., Reid, D., Richmond, B., 2009. Rates and trends of coastal change in California and the regional behavior of the beach and cliff system. J. Coast. Res. 25 (3), 603–615.
Hapke, C.J., Adams, P.N., Allan, J., Ashton, A., Griggs, G.B., Hampton, M.A., Kelly, J., Young, A.P., 2014. The rock coast of the USA. Memoirs 40. Geological Society: London, Chapter 9, pp. 137–154.
Hicks, D.M., Inman, D.L., 1987. Sand dispersion from an ephemeral river delta on the central California coast. Mar. Geol. 77, 305–318.
Höhle, J., Höhle, M., 2009. Accuracy assessment of digital elevation models by means of robust statistical methods. ISPRS J. Photogramm. Remote Sens. 64, 398–406.
Hungr, O., Evans, S., Hazzard, J., 1999. Magnitude and frequency of rock falls and rock slides along the main transportation corridors of southwestern British Columbia. Can. Geotech. J. 36, 224–238.
Juel, A., Groom, G.B., Svenning, J.-C., Ejrnæs, R., 2015. Spatial application of Random Forest models for fine-scale coastal vegetation classification using object based analysis of aerial orthophoto and DEM data. Int. J. Appl. Earth Obs. Geoinf. 42, 106–114.
Katz, O., Reches, Z., Roegiers, J.C., 2000. Evaluation of mechanical rock properties using a Schmidt hammer. Int. J. Rock Mech. Min. Sci. 37, 723–728.
Larsen, I.J., Montgomery, D.R., Korup, O., 2010. Landslide erosion controlled by hillslope material. Nat. Geosci. 3 (4), 247–251.
Letortu, P., Costa, S., Maquaire, O., Delacourt, C., Augereau, E., Davidson, R., Suanez, S., Nabucet, J., 2015. Retreat rates, modalities and agents responsible for erosion along the coastal chalk cliffs of Upper Normandy: the contribution of terrestrial laser scanning. Geomorphology 245, 3–14.
Li, M., Im, J., Beier, C., 2013. Machine learning approaches for forest classification and change analysis using multi-temporal Landsat TM images over Huntington Wildlife Forest. GIScience Remote. Sens. 50 (4), 361–384.
Li, X., Cheng, X., Chen, W., Chen, G., Liu, S., 2015. Identification of forested landslides using Lidar data, object-based image analysis, and machine learning algorithms. Remote Sens. 7, 9705–9726.
Lim, M., Rosser, N.J., Allison, R.J., Petley, D.N., 2010. Erosional processes in the hard rock coastal cliffs at Staithes, North Yorkshire. Geomorphology 114, 12–21.
Limber, P.W., Patsch, K.B., Griggs, G.B., 2008. Coastal sediment budgets and the littoral cutoff diameter: a grain size threshold for quantifying active sediment inputs. J. Coast. Res. 24 (2B), 122–133.
Limber, P.W., Barnard, P.L., Vitousek, S., Erikson, L.H., 2018. A model ensemble for projecting multidecadal coastal cliff retreat during the 21st century. J. Geophys. Res. Earth Surf. 123, 1566–1589.
Liu, J.-K., Li, R., Deshpande, S., Niu, X., Shih, T.-Y., 2009. Estimation of blufflines using topographic Lidar data and orthoimages. Photogramm. Eng. Remote. Sens. 75 (1), 69–79.
Liu, Y., Gong, W., Hu, W., Gong, J., 2018. Forest Type Identification with Random Forest Using Sentinel-1A, Sentinel-2A, Multi-Temporal Landsat-8 and DEM Data. Remote Sens. 10, 946. https://doi.org/10.3390/rs10060946.
Ma, Q., Su, Y., Guo, Q., 2017. Comparison of canopy cover estimations from airborne LiDAR, aerial imagery, and satellite imagery. IEEE J. Sel. Top. Appl. Earth Observ. Remote Sens. 10 (9), 4225–4236.
Malamud, B.D., Turcotte, D.L., Guzzetti, F., Reichenbach, P., 2004. Landslide inventories and their statistical properties. Earth Surf. Process. Landf. 29, 687–711.
Marjanović, M., Kovačević, M., Bajat, B., Voženílek, V., 2011. Landslide susceptibility assessment using SVM machine learning algorithm. Eng. Geol. 123 (3), 225–234.
Martin, D., 2012. Evolution of the NSRS. New Hampshire Land Surveyors Association December 07, 2012. https://outside.vermont.gov/agency/vtrans/external/docs/geodetic/Evolution%20of%20NSRS%20NHLSA%202012.pdf (accessed 2021-03-04).
Maxwell, A.E., Strager, M.P., Warner, T.A., Zégre, N.P., Yuill, C.B., 2014. Comparison of NAIP orthophotography and RapidEye satellite imagery for mapping for mining and mine reclamation. GIScience Remote. Sens. 51 (3), 301–320.
Milan, D.J., Heritage, G.L., Large, A.R.G., Fuller, I.C., 2011. Filtering spatial error from DEMs: implications for morphological change estimation. Geomorphology 125, 160–171.
Moore, L.J., 2000. Shoreline mapping techniques. J. Coast. Res. 16 (1), 111–124.
Naylor, L.A., Stephenson, W.J., Trenhaile, A.S., 2010. Rock coast geomorphology: recent advances and future research directions. Geomorphology 114 (1–2), 3–11.
Nuth, C., Kääb, A., 2011. Co-registration and bias corrections of satellite elevation data sets for quantifying glacier thickness change. Cryosphere 5, 271–290.
Olsen, M.J., Wartman, J., McAlister, M., Mahmoudabadi, H., O'Banion, M.S., Dunham, L., Cunningham, K., 2015. To fill or not to fill: sensitivity analysis of the influence of resolution and hole filling on point cloud surface modeling and individual rockfall event detection. Remote Sens. 7, 12103–12134.
Oskin, M.E., Arrowsmith, J.R., Hinojosa-Corona, A., Elliott, A.J., Fletcher, J.M., Fielding, E.J., Gold, P.O., Gonzalez-Garcia, J.J., Hudnut, K.W., Liu-Zeng, J., Teran, O.J., 2012. Near-field deformation from the El Mayor-Cucapah earthquake revealed by differential LIDAR. Science 335, 702–705.
Palaseanu-Lovejoy, M., Danielson, J., Thatcher, C., Foxgrover, A., Barnard, P., Brock, J., Young, A., 2016. Automatic delineation of seacliff limits using lidar-derived high-resolution DEMs in Southern California. J. Coast. Res. SI76, 162–173.
Patsch, K., Griggs, G., 2006. Littoral Cells, Sand Budgets, and Beaches: Understanding California's Shoreline. Institute of Marine Sciences, University of California, Santa Cruz.
Patsch, K., Griggs, G., 2008. A sand budget for the Santa Barbara littoral cell, California. Mar. Geol. 252 (1–2), 50–61.
Pawka, S.S., 1983. Island shadows in wave directional spectra. J. Geophys. Res. 88 (C4), 2579–2591.
Payo, A., Jigena Antelo, B., Hurst, M., Palaseanu-Lovejoy, M., Williams, C., Jenkins, G., Lee, K., Favis-Mortlock, D., Barkwith, A., Ellis, M.A., 2018. Development of an automatic delineation of cliff top and toe on very irregular planform coastlines (CliffMetrics v1.0). Geosci. Model Dev. 11, 4317–4337.
Prémaillon, M., Regard, V., Dewez, T.J.B., Auda, Y., 2018. GlobR2C2 (global recession rates of coastal cliffs): a global relational database to investigate coastal rocky cliff erosion rate variations. Earth Surf. Dyn. 6, 651–668.
Reichenbach, P., Rossi, M., Malamud, B.D., Mihir, M., Guzzetti, F., 2018. A review of statistically-based landslide susceptibility models. Earth-Sci. Rev. 180, 60–91.
Richter, A., Faust, D., Maas, H.-G., 2013. Dune cliff erosion and beach width change at the northern and southern spits of Sylt detected with multi-temporal Lidar. Catena 103, 103–111.
Rosser, N.J., Petley, D.N., Lim, M., Dunning, S.A., Allison, R.J., 2005. Terrestrial laser scanning for monitoring the process of hard rock coastal cliff erosion. Q. J. Eng. Geol. Hydrogeol. 38, 363–375.
Rosser, N.J., Brain, M.J., Petley, D.N., Lim, M., Norman, E.C., 2013. Coastline retreat via progressive failure of rocky coastal cliffs. Geology 41, 939–942.
Santana, D., Corominas, J., Mavrouli, O., Garcia-Sellés, D., 2012. Magnitude–frequency relation for rockfall scars using a terrestrial laser scanner. Eng. Geol. 145, 50–64.
Sibson, R., 1981. A brief description of natural neighbor interpolation. Interpolating Multivariate Data. John Wiley & Sons, New York, pp. 21–36.
Slott, J.M., Murray, A.B., Ashton, A.D., Crowley, T.J., 2006. Coastline responses to changing storm patterns. Geophys. Res. Lett. 33.
Stanley, T., Kirschbaum, D.B., Pascale, S., Kapnick, S., 2020. Extreme precipitation in the Himalayan landslide hotspot. Satell. Precipitation Meas. 1087–1111.
Sunamura, T., 1992. Geomorphology of Rocky Coasts. John Wiley & Son Ltd.
Swirad, Z.M., Rees, W.G., 2015. Geomorphometric analysis of a rocky coastline: an example from Hornsund, Svalbard. Int. J. Geogr. Inf. Sci. 29, 1694–1717.
Swirad, Z.M., Rosser, N.J., Brain, M.J., Vann Jones, E.C., 2016. What controls geometry of rocky coasts at the local scale? J. Coast. Res. SI75, 612–616.
Swirad, Z.M., Rosser, N.J., Brain, M.J., 2019. Identifying mechanisms of shore platform erosion using Structure-from-Motion (SfM) photogrammetry. Earth Surf. Process. Landf. 44, 1542–1558.
Terefenko, P., Paprotny, D., Giza, A., Morales-Nápoles, O., Kubicki, A., Walczakiewicz, S., 2019. Monitoring cliff erosion with LiDAR surveys and Bayesian network-based data analysis. Remote Sens. 11, 843.
Trenhaile, A.S., 1987. The Geomorphology of Rock Coasts. Oxford University Press.
Turowski, J.M., Cook, K.L., 2017. Field techniques for measuring bedrock erosion and denudation. Earth Surf. Process. Landf. 42, 109–127.
U.S. Army Corps of Engineers, 1971. National Shoreline Study California Regional Inventory. USACE South Pacific Division, San Francisco.
Vaughan, T.W., 1932. Rate of sea cliff recession on the property of the Scripps Institution of Oceanography at La Jolla, California. Science 75, 250.
Vos, K., Harley, M.D., Splinter, K.D., Walker, A., Turner, I.L., 2020. Beach slopes from satellite-derived shorelines. Geophys. Res. Lett. 47 (14), e2020GL088365.
Walkden, M., Dickson, M., 2008. Equilibrium erosion of soft rock shores with a shallow or absent beach under increased sea level rise. Mar. Geol. 251, 75–84.
Warrick, J.A., Ritchie, A.C., Schmidt, K.M., Reid, M.E., Logan, J., 2019. Characterizing the catastrophic 2017 Mud Creek landslide, California, using repeat structure-from-motion (SfM) photogrammetry. Landslides 16, 1201–1219.
Westoby, M., Lim, M., Hogg, M., Dunlop, L., Pound, M., Strzelecki, M., Woodward, J., 2020. Decoding complex erosion responses for the mitigation of coastal rockfall hazards using repeat terrestrial LiDAR. Remote Sens. 12, 2620.
Wheaton, J.M., Brasington, J., Darby, S.E., Sear, D.A., 2010. Accounting for uncertainty in DEMs from repeat topographic surveys: improved sediment budgets. Earth Surf. Process. Landf. 35, 136–156.
Williams, R.D., 2013. DEMs of difference. In: Clarke, L. (Ed.), Geomorphological Techniques. British Society for Geomorphology, London.
Williams, J.G., Rosser, N.J., Hardy, R.J., Brain, M.J., Afana, A.A., 2018. Optimising 4-D surface change detection: an approach for capturing rockfall magnitude–frequency. Earth Surf. Dyn. 6, 101–119.
Williams, J.G., Rosser, N.J., Hardy, R.J., Brain, M.J., 2019. The importance of monitoring interval for rockfall magnitude-frequency estimation. J. Geophys. Res. Earth Surf. 124, 2841–2853.
Woodroffe, C.D., 2002. Coasts: Form, Process and Evolution. Cambridge University Press.
Young, A.P., 2018. Decadal-scale coastal cliff retreat in southern and central California. Geomorphology 300, 164–175.
Young, A.P., Ashford, S.A., 2006. Application of airborne LIDAR for seacliff volumetric change and beach-sediment budget contributions. J. Coast. Res. 22, 307–318.
Young, A.P., Carilli, J.E., 2019. Global distribution of coastal cliffs. Earth Surf. Process. Landf. 44, 1309–1316.
Young, A.P., Flick, R.E., Gutierrez, R., Guza, R.T., 2009. Comparison of short-term seacliff retreat measurement methods in Del Mar, CA. Geomorphology 112, 318–323.
Young, A.P., Olsen, M.J., Driscoll, N., Flick, R.E., Gutierrez, R., Guza, R.T., Johnstone, E., Kuester, F., 2010a. Comparison of airborne and terrestrial lidar estimates of seacliff erosion in southern California. Photogramm. Eng. Remote. Sens. 76 (4), 421–427.
Young, A.P., Raymond, J.H., Sorenson, J., Johnstone, E.A., Driscoll, N.W., Flick, R.E., Guza, R. T., 2010b. Coarse sediment yields from seacliff erosion in the Oceanside Littoral Cell. J. Coast. Res. 26 (3), 580–585.

Young, A.P., Guza, R.T., O'Reilly, W.C., Flick, R.E., Gutierrez, R., 2011. Short-term retreat statistics of a slowly eroding coastal cliff. Nat. Hazards Earth Syst. Sci. 11, 205–217.
Young, A.P., Guza, R.T., O'Reilly, W.C., Burvingt, O., Flick, R.E., 2016. Observations of coastal cliff base waves, sand levels, and cliff top shaking. Earth Surf. Process. Landf. 41 (11), 1564–1573.
Young, A.P., Flick, R.E., Gallien, T.W., Giddings, S.N., Guza, R.T., Harvey, M., Lenain, L., Ludka, B.C., Melville, W.K., O'Reilly, W.C., 2018. Southern California coastal response to the 2015–2016 El Niño. J. Geophys. Res. Earth Surf. 123, 3069–3083.
Young, A.P., Guza, R.T., Matsumoto, H., Merrifield, M.A., O'Reilly, W.C., Swirad, Z.M., 2021. Three years of weekly observations of coastal cliff erosion by waves and rainfall. Geomorphology 375, 107545.